communications biology

A Nature Portfolio journal

Article

https://doi.org/10.1038/s42003-025-07866-7

Open-transmit and flexible receiver array for high resolution ultrahigh-field fMRI of the human sensorimotor cortex

Zidong Wei[1,2,3,4,8], Zhilin Zhang[5,8], Qiaoyan Chen[1,3], Cuiting Wang[4], Shuyue Fu[5,6], Haifeng Wang[1,3], Xiaoliang Zhang[7], Xin Liu[1,3], Hairong Zheng[1,3], Jinglong Wu[5] ✉ & Ye Li[1,3] ✉

In this study, we developed an open-transmit and 24-channel flexible receiver head coil assembly tailored for high-resolution ultrahigh-field functional magnetic resonance imaging (fMRI) of the human somatosensory and motor cortex. Leveraging the increased signal-to-noise ratio (SNR) and spatial resolution of ultrahigh field MRI, we address the technical challenges inherent in fMRI coil design. The open-birdcage transmit coil enhances patient comfort and enables visual task implementation, demonstrating superior performance in transmit efficiency and specific absorption rate distribution compared to conventional coils. Furthermore, the 24-channel flexible receiver head coil offers enhanced SNR and image quality, facilitating sub-millimeter vascular-space-occupancy imaging for precise functional mapping. These advancements provide valuable tools for unraveling the intricacies of somatosensory and motor cortex function. By enriching human brain functional studies, they contribute significantly to our understanding of the mechanisms underlying somatosensory and motor cortex function and may have valuable clinical applications in neurology and neuroscience research.

Humans possess excellent sensorimotor abilities that have a remarkable capacity for individualization and specialization through experience and training. The orchestration of these sensorimotor functions primarily occurs within the precentral and postcentral gyri, which form part of the primary sensory and motor areas of the brain[1–3]. Extensive research has elucidated the functions of cortical regions such as the occipital (visual), temporal (auditory), and prefrontal cortex (cognitive)[4], and more recently, the somatosensory and motor cortex has similarly begun to be intensively explored[5]. A deeper understanding of the somatosensory and motor cortex holds promise for clarifying the fundamental mechanisms underlying human behavior and action.

One seminal contribution to the study of the somatosensory and motor cortex was the conception of the cortical homunculus, a foundational representation in neuroscience. Beginning in the 1930s, Penfield and his colleagues mapped the human somatosensory and motor cortex with direct cortical stimulation, eliciting somatosensory and motor processing from about half of the sites, mostly from the foot, hand, and mouth[6–8]. This rough cortical map provided a textbook view of the somatosensory and motor organization as a continuous homunculus from head to toe, but a more precise system for characterizing the somatosensory and motor cortex was there, hiding in plain sight[9].

Functional magnetic resonance imaging (fMRI), the predominant methodology in modern neuroimaging with non-invasive in vivo functional mapping, provides high-quality imaging of the cortex[10]. It is most commonly performed using blood-oxygen-level dependent (BOLD) contrast[11]. Neuronal activity is followed by a reliable influx of oxygenated hemoglobin molecules that alters the ratio between oxygenated and deoxygenated hemoglobin molecules in the local blood supply. Due to oxygen's role in masking the magnetic field of hemoglobin, this changing ratio changes the local magnetic field surrounding the neural activity, which can be captured as BOLD. Although BOLD fMRI represents a modern approach to non-invasively mapping somatotopic activations based on the somatosensory and motor task, there remains a lack of high spatial resolution for facilitating more precise, whole-body somatotopic mapping[12–15]. Vascular space occupancy (VASO) is another fMRI method that measures cerebral blood volume (CBV) changes noninvasively through selective detection of signal changes in the extravascular compartment that are concurrent with the changes in the nulled blood compartment[16–19]. Compared with BOLD fMRI,

[1]Lauterbur Imaging Research Center, Shenzhen Institute of Advanced Technology, Chinese Academy of Sciences, Shenzhen, China. [2]University of Chinese Academy of Sciences, Beijing, China. [3]Key Laboratory for Magnetic Resonance and Multimodality Imaging of Guangdong Province, Shenzhen, China. [4]Shanghai United Imaging Healthcare, Shanghai, China. [5]Research Center for Medical AI, Shenzhen Institute of Advanced Technology, Chinese Academy of Sciences, Shenzhen, China. [6]School of Medical Technology, Beijing Institute of Technology, Beijing, China. [7]Department of Biomedical Engineering, University at Buffalo,the State University of New York, Buffalo, NY, USA. [8]These authors contributed equally: Zidong Wei, Zhilin Zhang. ✉e-mail: jl.wu@siat.ac.cn; liye1@siat.ac.cn

VASO fMRI can provide higher spatial specificity making laminar fMRI more specific and robust across different cortical depths. It can thus be surmised that combination of these two fMRI techniques, could yield a more precise means of visualizing somatosensory and motor cortex.

Ultrahigh-field MRI (>3T) offers significant improvement in both imaging signal-to-noise ratio (SNR) and functional signal contrast-to-noise ratio, thus providing high spatial resolution for the visualization of sub-millimeter cortical columns and subnuclei structures in fMRI. However, as the magnetic field strength of MRI systems increases, the RF wavelength becomes shorter and the radio frequency (RF) transmit field (B_1^+) inhomogeneous. Moreover, the specific absorption rate (SAR) increases quadratically with the magnetic field strength. To mitigate these problems, local transmit coils are commonly used[20,21]. The transmit array element types include birdcages[20], loops[22,23], microstrip transmission lines[24–26], dipole antennas[27–30], sleeve antennas[31] and hybrid arrays[32,33]. In the designs of birdcages and loops, RF shielding has proven indispensable in reducing radiation loss, which reduces the comfort of the subject during the MRI scan, especially those with claustrophobia. Similarly, the individual microstrip transmission line consists of a strip with a narrow width and a ground plane separated by a low-loss dielectric substrate with thickness. These closed structures are not conducive to performing cognitive MRI experiments, especially the visual fMRI[34]. To provide an opening in the front of the participants' faces, half-volume RF transmit coils[35,36], asymmetric dipole, and sleeve antenna arrays[31] can be applied. However, the RF transmit field area of these designs does not produce a homogeneous excitation. Moreover, for the phased-array transmit coils, the coupling between them is complicated[37,38]. To address these abovementioned issues, Nikulin et al. designed a more open system by reducing the number of legs on the birdcage coil and opening holes in the shield. However, this approach resulted in a decrease in the uniformity of the transmit field distribution and excitation efficiency[39].

In human brain studies, the RF receiver coils have typically been designed with a higher density of coil elements laid out on top of a headshell, which can improve the SNR and parallel acceleration capacity. The channel number has been increased from 32 to 64 or to even as high as 128[40–44]. These designs are based on an adaptive rigid shell, the coil elements of which are located at a specified distance from the imaging position. The flexible head coils have demonstrated certain advantages in terms adaptability and SNR[45–50]. Therefore, for fMRI, the design should include a flexible receiver head coil with an open-face birdcage coil.

In this study, we designed and constructed an open-transmit and 24-channel flexible receiver head coil assembly for human somatosensory and motor cortex fMRI at 5T. This local open-transmit coil design with a facial open-window birdcage is intended to both increase patient comfort and enable observation of fMRI stimuli. Using simulations, we compared the facial open-window birdcage coils with two different configurations and a conventional shielded birdcage coil in terms of transmit efficiency, B_1^+ uniformity, and SAR efficiency. The 24-channel flexible receiver head coil was additionally designed for high–spatiotemporal resolution fMRI of the cortical regions to maximize imaging SNR and parallel imaging performance. A series of coil performance evaluations were implemented, in which both high-resolution structural and functional scans were performed of the somatosensory and motor region, with our design being compared to a quadrature birdcage transmit, 48-channel receiver coil assembly[43].

Results

Bench test results

The measured Q_{ratio} of the 40-mm diameter loop with surrounding elements was 2.82 (90/32). For comparison, when the surrounding elements and components were eliminated, the isolated loop Q_{ratio} increased to 3.93 (118/30). The *Q*-factor metrics of the Rx array were measured and verified

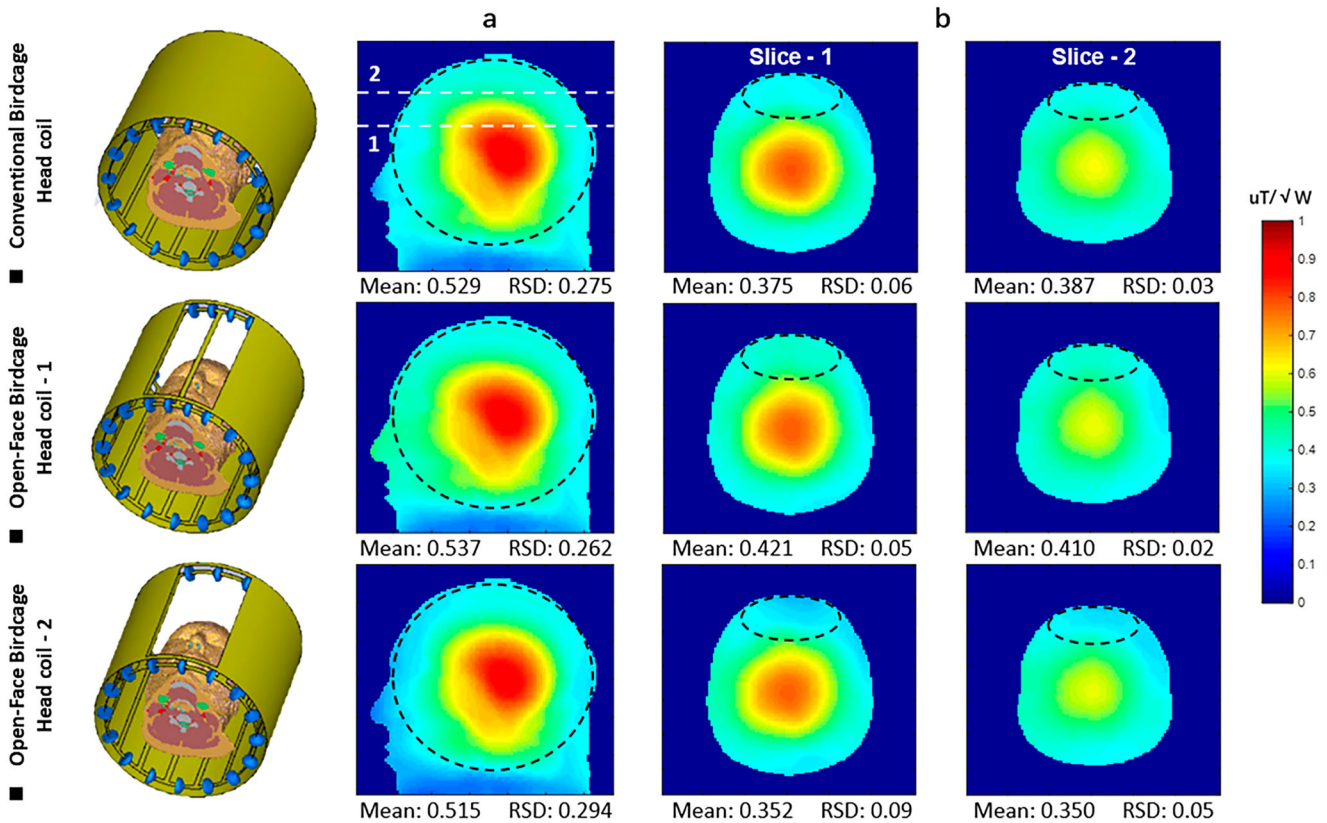

Fig. 1 | The electromagnetic-simulated B_1^+ field maps of the different birdcage coils without the receiver arrays. a The simulated B_1^+ field maps in the sagittal plane. **b** The simulated B_1^+ field maps in two transversal planes. The improved open-face birdcage provided a 15.3% higher transmit efficiency compared to the other open-face configuration and a 7.3% higher transmit efficiency compared to the standard shielded birdcage, particularly in front of the brain region. RSD relative standard deviation.

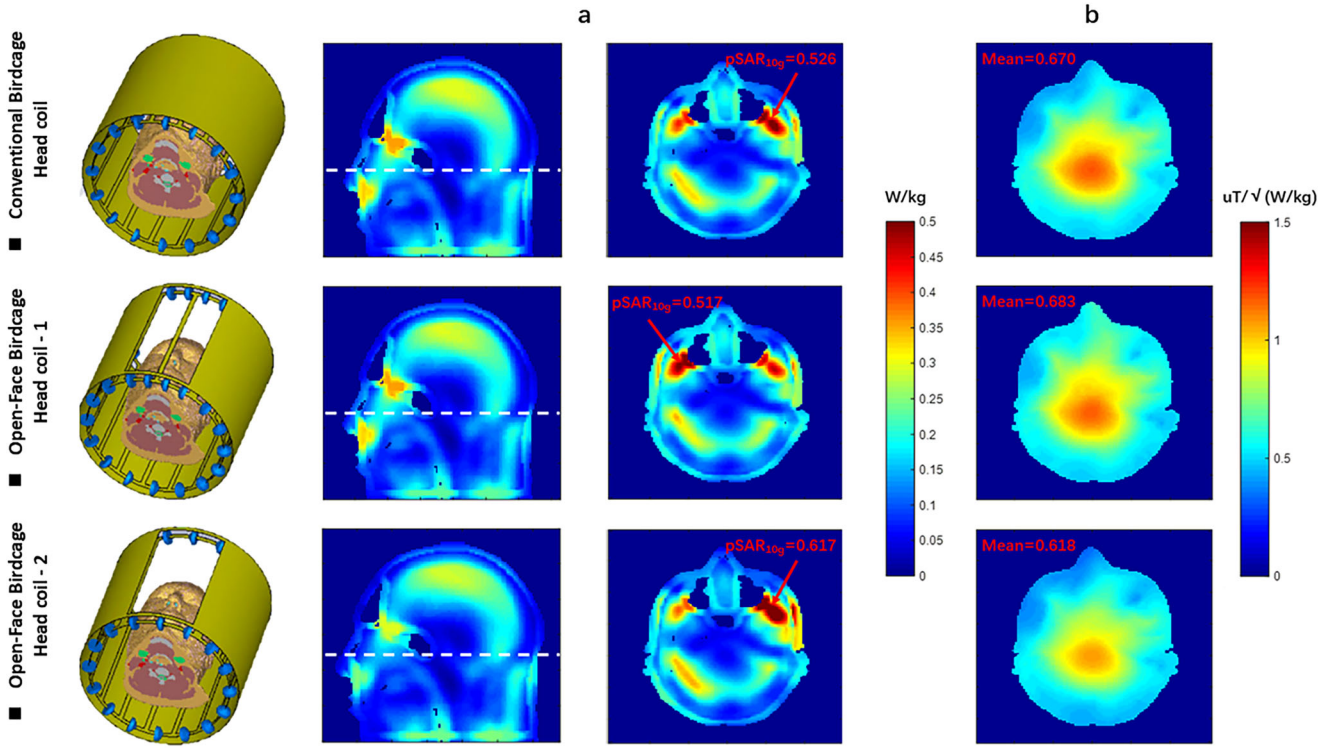

Fig. 2 | The SAR_{10g} maps and the SAR efficiency maps of the different birdcage coils. a The SAR_{10g} maps and the local peak SAR_{10g} values of the different birdcage coils. **b** The SAR efficiency maps of the different birdcage coils. The improved open-face birdcage demonstrated a 10.5% better SAR efficiency compared to the initial open-face birdcage coil and was comparable to the 16-rung standard birdcage coil. SAR specific absorption rate.

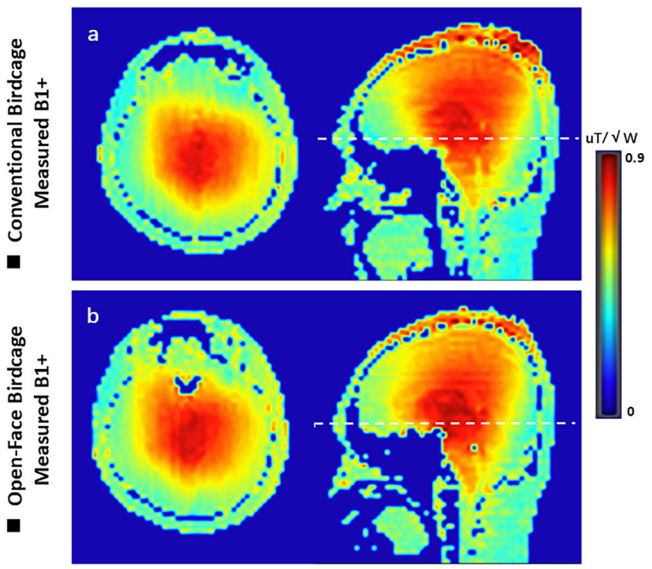

Fig. 3 | The measured B_1^+ field maps of the different birdcage coils. a The measured B_1^+ field maps of the conventional shielded birdcage. **b** The measured B_1^+ field maps of the open-face birdcage. The open-face birdcage transmit coil demonstrated a superior transmit efficiency in the prefrontal region of brain compared to the conventional birdcage coil, while the B_1^+ field distribution in the other regions was similar.

before and after the addition of the detuned Tx structure, revealing a slight decrease in the unloaded *Q*-factor of the Rx elements. All Rx elements were tuned to the Larmor frequency at 210.8 MHz, and matching levels below −10 dB were achieved for all Rx elements when loading was completed with a head-and-neck phantom on the bench. By using the geometry overlap decoupling method, the decoupling of adjacent pairs of Rx loops ranged from −12 dB to −19 dB, demonstrating that the coil elements were well-tuned and matched. The worst-case decoupling of non-adjacent pairs of Rx loops was −6.7 dB by only using the preamplifier decoupling method. Active positive-intrinsic-negative (PIN) diode detuning provided a nearly 40 dB isolation between the tuned and detuned states

The open-transmit birdcage coil was tuned to 210.8 MHz and matched to 50 Ω, with a reflection parameter of less than −10 dB. The isolation between the two feeding ports was adjusted and measured to be at least −10 dB in the loaded condition.

Electromagnetic simulations

Figure 1 shows the simulated B_1^+ maps in the sagittal plane and two representative transversal planes. The mean and relative standard deviation (RSD) values of the transmit efficiency in the region of interest (ROI) are respectively depicted in the maps. As indicated by the quantitative data, the transmit efficiencies over the sagittal planes were comparable (within 5%) for all coils. In the two representative transversal planes, the results show that the improved open-face birdcage provided a 15.3% higher transmit efficiency as compared to the other open-face configuration, and a 7.3% higher transmit efficiency as compared to the standard shielded birdcage, particularly in front of the brain region. The RSD values in the ROI depicted the ellipses suggest that the improved open-face birdcage had a more uniform field than did the standard shielded birdcage and the other open-face configuration in both the sagittal plane and two transversal planes.

The SAR_{10g} maps and the local peak SAR_{10g} values are shown in Fig. 2a. The improved open-face birdcage showed the best SAR efficiency, as shown in Fig. 2b. The improved open-face birdcage demonstrated a 10.5% higher SAR efficiency compared to the initial open-face birdcage coil and comparable to the 16-rung standard birdcage coil.

Figure 3 shows the measured B_1^+ maps of the conventional shielded birdcage and improved open-face birdcage coils. The open-face birdcage

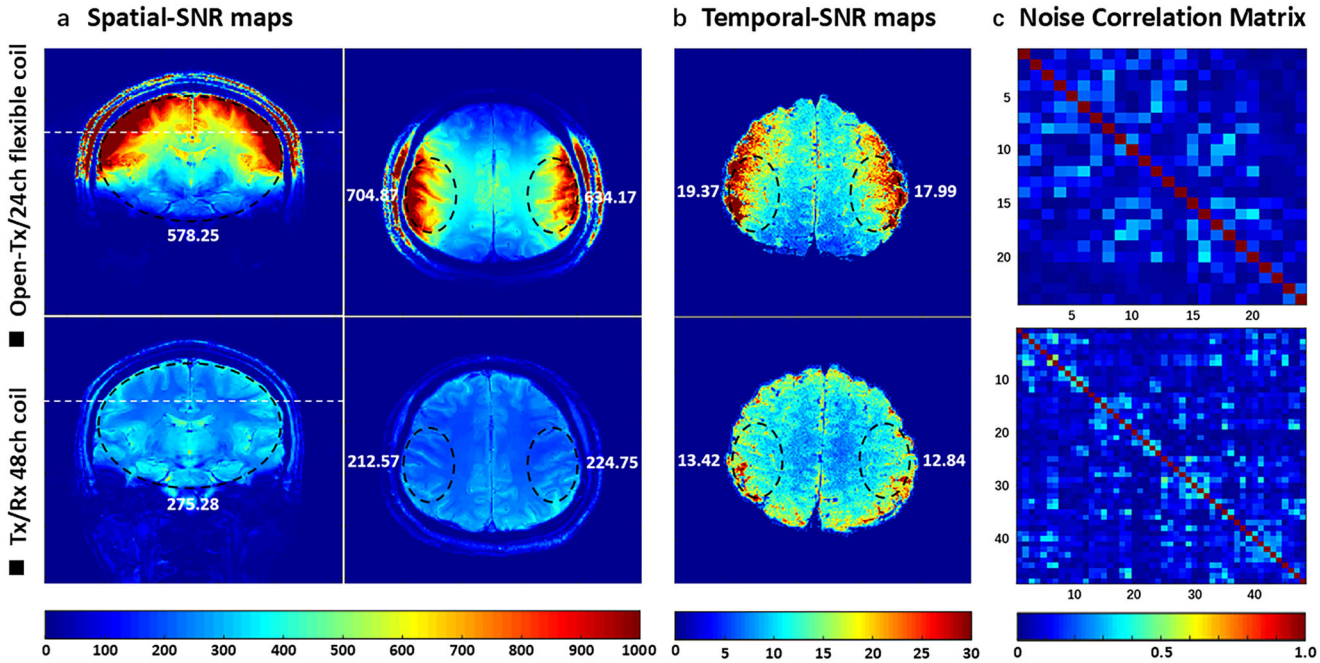

Fig. 4 | The in vivo spatial SNR maps, temporal SNR maps, and noise correlation matrix for the proposed 24-channel flexible coil and 48-channel head coil. a The in vivo spatial SNR maps. **b** the temporal SNR maps. The proposed receiver coil could provide an up to threefold improvement in the SNR in the cortex region and a superior temporal-SNR value than could the 48-channel head coil. **c** The noise correlation matrix of the 24-channel flexible proposed coil and 48-channel head coil in human studies. The maximum and mean values of the noise correction matrix with exception for the diagonal elements are shown below the maps. These results indicate sufficient channel decoupling.

transmit coil demonstrated a superior transmit efficiency in the prefrontal region of the brain compared to the conventional birdcage coil, while the B_1^+ field distribution in the other regions was similar.

In vivo human brain imaging

To validate the coil decoupling, the noise correlation matrix of the 24-channel flexible proposed coil and the 48-channel head coil was calculated, as shown in Fig. 4b. The maximum and mean values of the noise correlation matrix, except for the diagonal elements, are shown below the maps. For the proposed receiver coil, the mean and maximum values of the noise correlation with the exception of the diagonal elements were 8.2% and 34.8%, respectively, and were 9.5% and 50.3% for the 48-channel receiver coil, respectively. Figure 4b also shows results demonstrating that using the geometry overlap and preamplifier decoupling method could provide sufficient channel decoupling.

Figure 4a shows the spatial-SNR maps with flip-angle correction and the temporal-SNR maps in transversal plane of the human brain. The mean values of SNR in the ROIs are depicted in the maps. The proposed receiver coil could provide an up to threefold improvement in the SNR in the cortex region and a superior temporal-SNR value than the 48-channel head coil.

The inverse g-factor maps in the transverse plane with various sensitivity encoding acceleration factors in both the anterior-posterior (A-P) direction and right-left (R-L) directions. The A-P and R-L directions are shown in Fig. 5, with the green and red numbers in brackets indicating the mean and maximum *g*-factor values in the brain region, respectively. Therefore, as indicated by the mean and maximum g-factors in the brain region, the parallel imaging capability of the 24-channel flexible proposed coil was superior to that of the 48-channel head coil, particularly at high acceleration factors.

Figure 6 shows the T2*-weighted brain images with a high resolution of $0.2 \times 0.2 \times 1\ mm^3$ from the proposed coil assembly and quadrature birdcage transmit/48-channel receiver coil assembly. Aspects of the submillimeter structure, such as small cortical blood vessels, were more clearly visualized with the proposed coil assembly.

BOLD fMRI evaluation

In the human motor task with the BOLD sequence, we found finger-tapping-induced activation in the primary motor cortex and the somatosensory cortex. Functional MRI data was acquired at 0.8 mm isotropic resolution using the Tx/Rx 48ch coil and the Open-Tx/24ch flexible coil, as shown in the Fig. 7 activity maps. The maps are thresholded to the same Z value (2–14) across both coils. Through a combination of a closely spaced loop and densely packed receiver coils in the regions of interest, the resulting activation of the Open-Tx/24ch flexible coil conformed to a stronger pattern, indicating that notwithstanding the small voxel size, fMRI responses could be measured adequately if appropriate imaging hardware were used.

VASO fMRI evaluation

In the human motor task with the VASO sequence, we found that the finger-tapping submillimeter VASO imaging setup could reliably capture neurally induced functional CBV changes in the primary motor cortex. It was observed that under using the Open-Tx/24ch flexible coil and the Tx/Rx 48ch coil, the activity was confined to the gray matter, with no sensitivity to the large drain pial veins above the gray matter surface. Compared with the Tx/Rx 48ch coil, the CBV maps of the Open-Tx/24ch flexible coil indicated more clearly depict the activity in the superficial and the deep cortical layers (Fig. 8). These results indicated that the Open-Tx/24ch flexible coil could be used for mapping of laminar activity in human primary motor cortex.

Discussion

In this study, an open-face birdcage transmit coil was designed and compared with a traditional birdcage transmit coil. The opening structure of the birdcage coil could affect the excitation efficiency and SAR distribution. Through optimized design, better excitation efficiency and lower SAR distribution were achieved with the open birdcage transmit coil. This open-face birdcage transmits coil can not only support visual tasks of brain function but may also alleviate the clinical experience of claustrophobia, which provides a novel and feasible means for conducting whole-brain functional imaging in ultrahigh-field MRI.

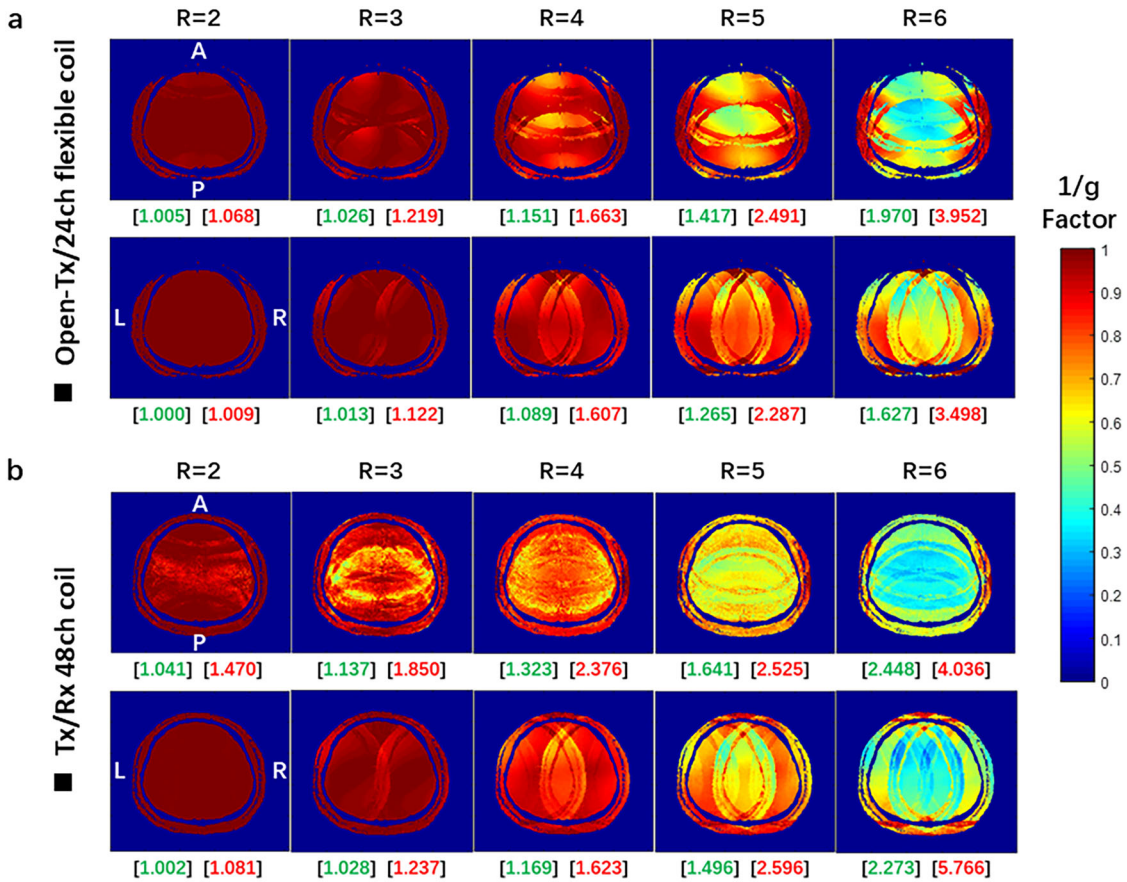

Fig. 5 | The inverse g-factor maps in the transversal plane of the human brain for the proposed 24-channel flexible coil and 48-channel head coil. a The inverse *g*-factor maps for the proposed 24-channel flexible coil. **b** The inverse *g*-factor maps for the 48-channel head coil. The green and red numbers in brackets indicate the mean and maximum *g*-factor values in the brain region, respectively. The parallel imaging capability of the 24-channel flexible proposed coil was superior to that of the 48-channel head coil, particularly at high acceleration factors.

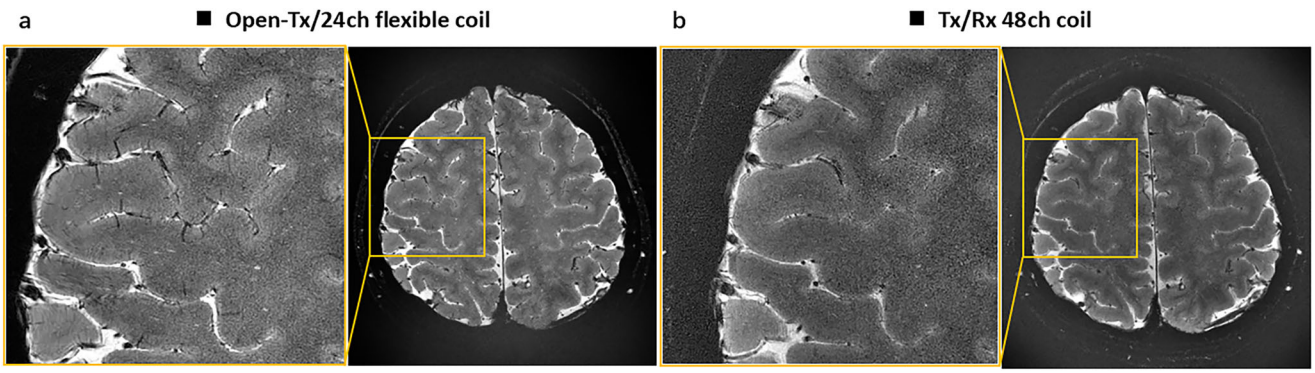

Fig. 6 | High-resolution (0.2 mm in plane) gradient-echo T2*-weighted images of a healthy volunteer (24-year-old female; 168 cm; 50 kg). a T2*-weighted images obtained using the proposed coil assembly. **b** T2*-weighted images obtained using the Tx/Rx 48ch coil. Aspects of the submillimeter structure, such as small cortical blood vessels, were more clearly visualized with the proposed coil assembly.

Another method that can achieve an open transmit coil is the use of phased-array transmitting coils. However, due to the coupling between the coil elements, the design and circuits of the phased-array transmitting coils are more complicated than are those of the birdcage coil. Moreover, the birdcage coil structure advantageous in terms of transmit field homogeneity.

The human somatosensory and motor cortex has a particularly small cortical thickness of only 2–3 mm and a relatively fine-scale organization[17]. Despite evidence indicating this cortex is involved in tasks across the cognitive domain, the particularities of its composition have led to a scarcity of high-resolution fMRI studies. Increasing the fMRI resolution, optimizing the SNR, and further improving sensory and motor cortex anatomical imaging may help in this regard. In this study, the 24-channel flexible receiver head coil was closer to the imaging region than the 48-channel head coil with fixed construction. Therefore, a higher SNR could be obtained. Moreover, the 24-channel flexible coil had a higher density distribution in the transverse plane for the inverse g-factor maps than did the 48-channel coil. Therefore, the parallel imaging capability of the proposed 24-channel flexible coil was superior to that of the 48-channel head coil in the

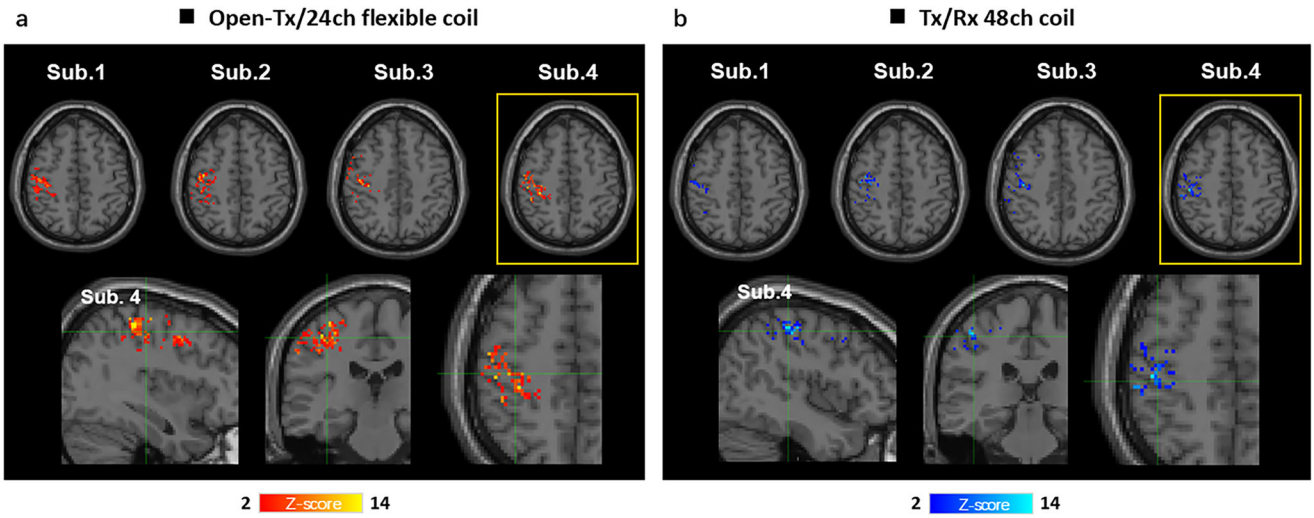

Fig. 7 | The BOLD fMRI activation maps of representative subjects. a The BOLD fMRI activation maps without smoothing from four subjects for the Open-Tx/24ch flexible coil at 0.8 mm isotropic. **b** The BOLD fMRI activation maps without smoothing from four subjects for the Tx/Rx 48ch coil at 0.8 mm isotropic.

Fig. 8 | Layer-fMRI profiles in the primary motor cortex for VASO in representative subjects. a The layer-dependent fMRI responses without smoothing from four subjects for the Tx/Rx 48ch coil and the Open-Tx/24ch flexible coil in the primary motor cortex. **b** The imaging slice is aligned perpendicular to the cortical surface of the right-hand representation in the left motor cortex. **c** The average cortical profiles across all participants show laminar patterns in superficial and deep cortical laminae for the finger-tapping task. Shaded areas refer to the SEM across participants. CBV cerebral blood volume, WM white matter, CSF cerebrospinal fluid.

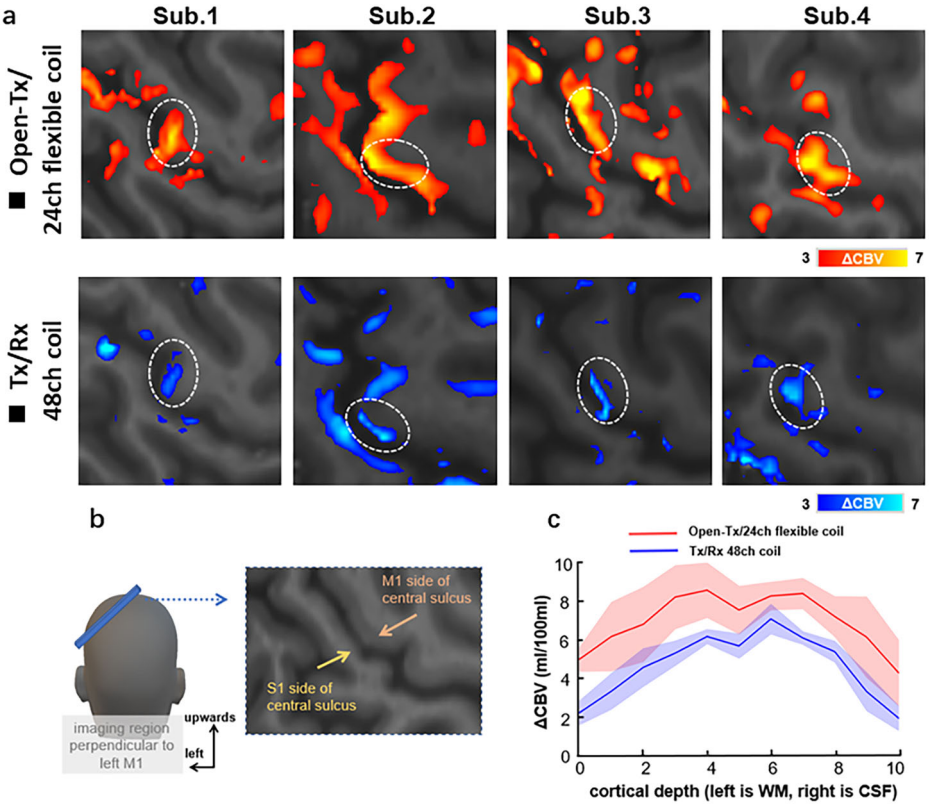

presentation of the transverse plane, particularly at high acceleration factors. Liquid metal wires, coaxial cables, and other flexible wires can be applied to realize the flexible head coil. In the layout design of the receiver coil, elements 1 and 2, which laid on the top of head, also contributed to the SNR. The 24-channel flexible coil was designed mainly for human somatosensory and motor cortex fMRI, which had 24 closely spaced loops with a diameter of 40-mm distributed on the top and the two sides of the head. Meanwhile, the 48-channel coil was designed for whole-brain imaging including the cerebellum. The sizes of each loop element of the 48-channel receiver coil are 65–75 mm in length. The smaller the diameter of the 24-channel flexible receiver head coil, the higher its sensitivity. Similar to the 48-channel coil designed for whole-brain imaging, a 32-channel receive loop combined with an 8-channel dipole coil array was constructed for 7T MRI[27]. In this design, the larger loop coil has a size of 88 × 60 mm, while the smaller one has a size of 68 × 30 mm. This coil array could achieve the integration of high-resolution MR imaging with simultaneous left and right auditory functions with fMRI[51].

The human somatosensory and motor cortex are reciprocally connected. The reciprocal interaction between the somatosensory and motor cortex is crucial for haptic perception and movement[52]. However, the mechanism underlying the interaction between the somatosensory and motor cortices is usually required to localize the somatotopic representations between sensory inputs and motor responses of the fingers for each participant, where individual fingers are represented in only a few voxels[53].

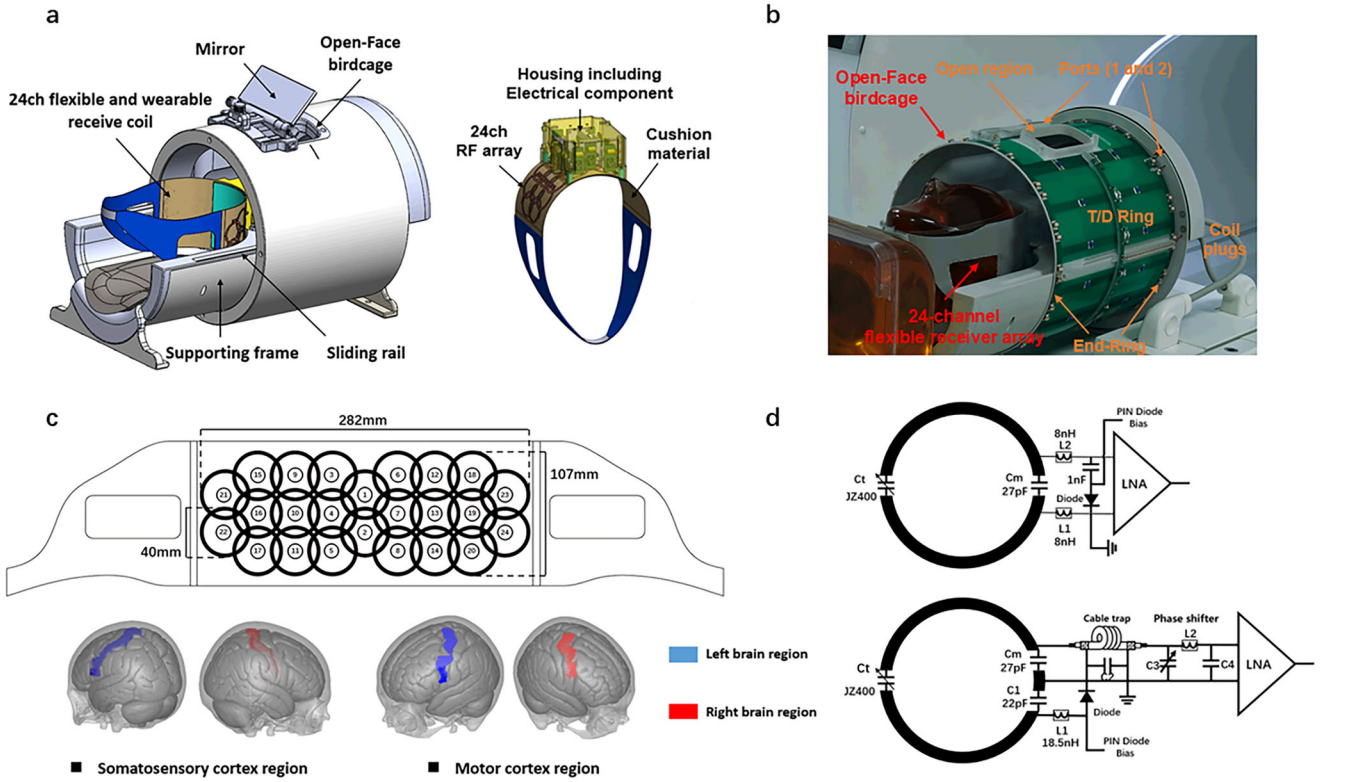

Fig. 9 | The open transmit and 24-channel flexible receiver coil assembly at 5 T. **a** The 3D rendering of the constructed open transmit/24ch flexible coil assembly. **b** Photograph of the proposed coil with the RF shielding removed. **c** Layout of the 24-channel receive coil and location of human somatosensory and motor cortex. **d** The circuit schematic of the receiver coil element.

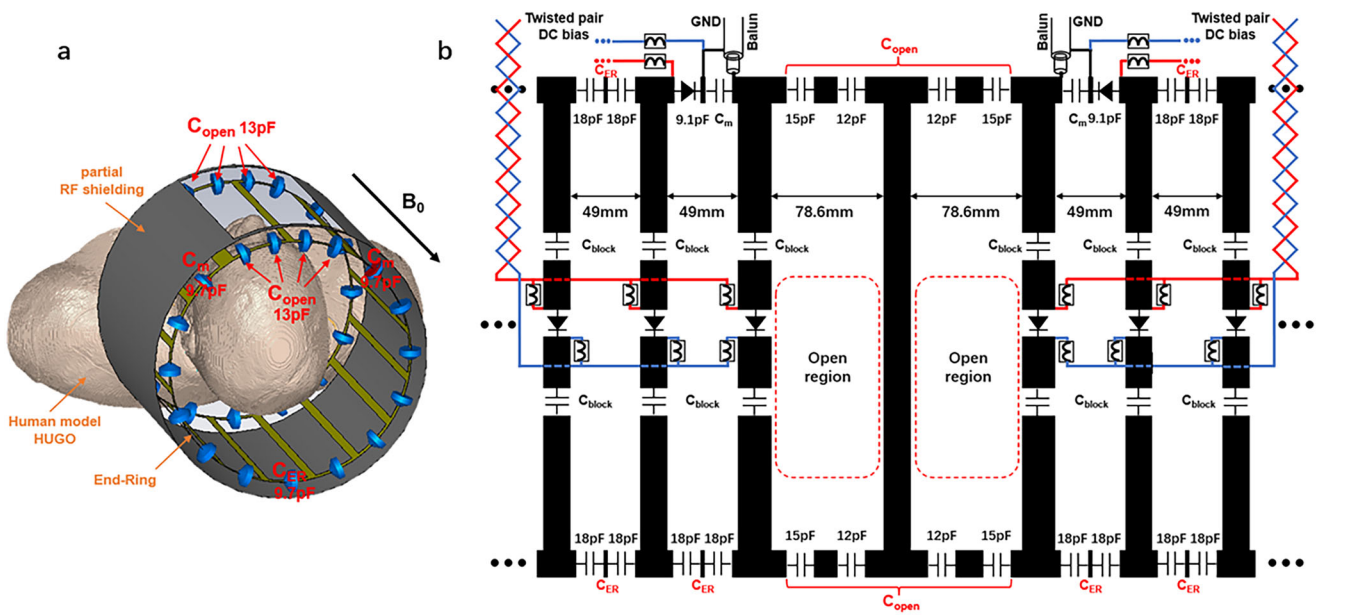

Fig. 10 | The circuit schematics of the open-face birdcage coil. **a** The circuit schematics for simulation. **b** The circuit schematics for simulation experimental.

Some studies have shown that the fMRI signal is roughly proportional to the measurement of local neural activity, and the relationship between the signal and the underlying neural activity depends on the fMRI acquisition technique[54]. The stronger BOLD signal we obtained will facilitate future research into the localization of somatotopic finger mapping for each participant and the interaction between human somatosensory and motor systems.

Compared to 3T MRI systems, 5T MRI systems can provide significantly higher SNR[43]. Therefore, the submillimeter VASO imaging with a high resolution of 0.8 mm could be achieved at 5T, while this study cannot be achieved at 3T. Additionally, the 5T MRI achieved a more homogenous B_1^+ field and lower SAR than did the 7T MRI, and these are the main considerations of ultrahigh field MRI. Moreover, the open-transmit coil in this study was more patient-friendly for cognitive functional MRI

experiments compared to the closed birdcage transmit coils of the commercial 7T MRI systems.

In conclusion, an open-transmit and 24-channel flexible receiver head coil assembly was designed for in vivo cortical imaging of the human somatosensory and motor cortex in an ultrahigh field MR scanner. The open-face birdcage transmit coil could not only improve patient comfort but also facilitate the visualization of brain function. The open-face birdcage transmit coil demonstrated substantial improvements in transmit efficiency, $B1^+$ uniformity, and SAR efficiency when compared with a conventional shielded birdcage coil. The 24-channel flexible receiver head coil provided a higher SNR and better image quality in anatomical imaging and functional imaging than did the 48-channel head coil. Most importantly, clear CBV changes could be obtained in the submillimeter VASO imaging using the 24-channel flexible receiver head coil. These findings indicate that the open-transmit, 24-channel flexible receiver head coil assembly can be used for fMRI to clarify the mechanisms of the somatosensory and motor cortex and may thus be highly valuable for functional studies of the human brain.

Methods

RF coil design

Figure 9a, b is a 3D rendering and photograph, respectively of the open-face birdcage coil assembled with the 24-channel flexible receiver head coil. The open-face birdcage configuration was achieved by removing and adjusting the legs of the 16-rung high-pass birdcage coil on the anterior side. Additionally, an open window (measuring 14 × 28 cm) was created on the RF shielding to allow for an unobstructed view of the eyes. PIN diodes (Cat. No. MA4P7435NM-1091T; Macom) were integrated into all legs except for the leg adjacent to the facial open window and into each port of the transmit coil to facilitate active detuning in the receive mode. The circuit schematics of the open-face birdcage for simulation and experimental are illustrated in Fig. 10a, b, respectively. The receiver arrays were not included in the simulations. Two capacitors were set on the open ring. The simulated values were 13 pF and 13 pF, while the experimental values were 15 pF and 12 pF. The capacitors on the other rings were 9.7 pF in the simulation and 9 pF in the experiment, using two capacitors with a value of 18 pF in series. The matching capacitors were 9.7 pF in the simulation and 9.1 pF in the experiment. The open-transmit coil was driven in the circularly polarized mode.

The customized surface coil array was specifically designed for high spatiotemporal-resolution MRI/fMRI of the cortical region via 24 closely spaced loops with a diameter of 40-mm to maximize both the SNR and parallel imaging performance. The geometrical layout of the receiver loops was meticulously crafted to encompass the human somatosensory and motor cortex, as illustrated in Fig. 9c. The receiver coil elements were fabricated from 35 μm thick copper on a semi-flexible polyimide substrate and mounted on a flexible cushion. The overlap decoupling method was applied to cancel the inductive coupling between neighboring loops.

Additionally, the next-nearest neighboring loops were decoupled using the preamplifier decoupling method. Figure 9d shows the circuit schematic of the receiver coil element, comprising a tuning circuit, a matching circuit, and an active detune circuit. Elements 1–14 were soldered directly onto the FR4 PCB boards with a matching capacitor of 27 pF, which were then securely housed inside the PCB box. Active detuning was facilitated through the use of a PIN diode (Cobham, DH80055-40N) in series with inductors L1 and L2, resonating with capacitor Cm at the Larmor frequency of 210.8 MHz. When the PIN diode was forward-biased, the resonant parallel circuit introduced a high impedance in series with the loop. Conversely, when the PIN diode was reverse-biased, preamplifier decoupling was achieved, transforming the preamplifier input impedance (<2 Ω) into a high-impedance series within the loop. For surrounding coil elements 15–24, careful adjustments of cable length and phase shifter settings were made for each loop to ensure preamplifier decoupling, with matching capacitor of 27 pF. To minimize Hall effect issues within the field-effect transistors, all preamplifiers were oriented in the z-direction.

Bench measurements

The constructed open-transmit and 24-channel flexible receiver coil underwent adjustment and evaluation using standardized bench metrics under anthropomorphic head-and-neck phantom-loaded conditions. The phantom had a conductivity of 0.53 S/m and a relative permittivity of 55.4 at 210.8 MHz. Tuning, matching, active detuning, and decoupling of the receiver array coils were executed using a calibrated vector network analyzer (Agilent, E5061B) and a power supply. This power supply provided DC power (6.5 V) for the preamplifiers and facilitated manual switching of the PIN diode bias (150 mA/−30 V) supply for each receiver channel. The unloaded-to-loaded quality factor ratio (Q_{UL}/Q_L) for Rx elements was determined for an individual element with no cable attached using the S_{21} double-probe method[55]. The quality factor was calculated by dividing the center frequency by the −3 dB bandwidth (BW) of the S_{21} curve. For evaluating the tuning and matching of individual elements, S_{11} parameter values were measured using the vector network analyzer. To assess decoupling between two coil elements, S_{21} parameter values were measured on the vector network analyzer using cables directly connected to the preamplifier sockets. Throughout the decoupling test, all preamplifiers were connected to the custom-made power supply. Only two coil elements were tuned during the decoupling test, while all other coil elements were actively detuned with the PIN diode under forward bias.

The open-transmit birdcage was tuned to the Larmor frequency and matched to a 50 Ω impedance to ensure power-matched conditions under phantom loading. The power supply was also used to a provide current bias with a 150 mA current for tuning the transmit coil and detuning the receiver array during the transmit mode.

EM simulation and validation

In this study, an optimized open-face birdcage head coil was designed using electromagnetic (EM) simulations. The transmit efficiency, $B1^+$ uniformity, and SAR efficiency of the facial open-face birdcage coil were compared with those of two different configurations and a conventional shielded birdcage coil. Mean and RSD values were calculated in the two-dimensional (2D) ROIs. Finally, an optimized open-face birdcage head coil was built and validated on a whole-body 5T MRI scanner.

All the EM simulations were performed using the finite-integration time-domain method and RF circuit co-simulation for optimizing the capacitance values of the transmit coils in Microwave Studio software (CST, Darmstadt, Germany). The realistic human head voxel model (HUGO) was used for the EM simulation study. The dielectric parameters are based on the Gabriel dispersion relationships[56]. Three configurations were evaluated: (1) a conventional shielded high-pass birdcage with 16 rungs; (2) an initial open-face birdcage, in which the top two legs were removed from the conventional birdcage structure to achieve a view window on the top face; and (3) an improved open-face birdcage, which was designed based on the previous configuration with an addition leg at the top of the Open-Face window to improve transmit efficiency. All the configurations were driven in the circular polarized mode. Both the simulated B_1^+ field maps and SAR_{10g} maps were constructed by normalizing the accepted input power with 1 W. The open-face coils were tuned at 210.8 MHz by adjusting the capacitor values (except at the open window) on the end ring. The capacitance value on the open ring was optimized for both the open-face birdcage coils.

MRI and experimental preparation

To fully assess the proposed coil, we performed several human MRI experiments including (1) coil performance evaluation, (2) high-resolution structural brain imaging over somatosensory and motor cortex, and (3) high-resolution functional brain imaging with somatosensory and motor tasks. All experiments were performed using a novel whole body 5.0T MRI scanner (United Imaging Healthcare, Shanghai, China) with a 60-cm diameter clear bore. The field homogeneity of the main magnet was about 0.02 ppm over an empty sphere with a 20 cm diameter. The gradient system was driven by a 3.5 MW power amplifier, equipped with a maximum

gradient strength of 120 mT/m and a slew rate of 200 T/m/s. The scanner was equipped with 96 receivers and 8 parallel transmitters. Each transmitter was independently driven by an RF power amplifier, each with a peak power of 8 kW. Therefore, the total RF peak power of the scanner was 64 kW.

The experiments for coil performance evaluation and in vivo human brain study were implemented with four healthy volunteers. All of them were right-handed according to the Edinburgh Handedness Inventory (Oldfield 1971). All the participants were healthy; had normal visual, auditory, and tactile sensory function; and had no history of neurological or psychiatric dysfunction. The protocol and data collection of the study were approved by the ethics committee of Shenzhen Institute of Advanced Technology, Chinese Academy of Sciences in accordance with the Declaration of Helsinki. Written informed consent was obtained from each participant following a detailed explanation of the study.

In the human motor experiment, an individual tapping of two fingers (index and thumb) was interspaced with rest periods. This task engages muscle extension and muscle flexion of the index and the thumb fingers. The tapping frequency was self-paced at a frequency of approximately once every 1 s. The tapping timing was locked to scanner triggers in units of 10 times to relaxation (TRs) (TR = 3 s for the BOLD, TR = 4.7 s for the VASO) and contained visual cues when to tap which finger and for how long. Each run consisted of 10 TRs of task and 10 TRs of rest, repeated ten times. Motor tasks were performed with the right hand while the primary sensorimotor cortex was imaged on both sides of the central sulcus in the left hemisphere. The left hand was not engaged during any of the experiments of this study.

Data acquisition and analysis

In the B_1^+ field measurements, the receiver coils were assembled within the transmit coil. The B_1^+ maps were acquired using a dual refocusing echo acquisition mode (DREAM) sequence with the following parameters: time of relaxation (TR) = 3000 ms, time of echo (TE1/TE2) = 1.50/4.27 ms, flip angle = 54.7°, slice thickness = 10 mm, field of view (FOV) = 250 × 250 mm^2, and matrix size = 80 × 80. The simulated and measured B_1^+ field maps were constructed by normalizing the accepted input power with 1 W. In the MRI system, a directional coupler was used to measure and monitor the transmitted RF power. The directional coupler was connected in series at the transmit power amplifier to detect the forward power and reverse power. The measurement point was at the coil plug level. Notably, the measured B_1^+ field maps were constructed after a −4 dB transmission loss from the RF amplifiers to the coil plugs and a −0.3 dB loss from coil plugs to the matched transmit coil.

For spatial-SNR comparisons, a two-dimensional (2D) gradient echo (GRE) sequence was applied for signal acquisition with the following parameters: TR/TE = 1000/15 ms, BW = 130 Hz/pixel, slice thickness = 5 mm, FOV = 200 × 200 mm^2, and matrix size = 256 × 256. Noise images were acquired by setting the flip angle to zero. SNR maps were calculated using the sum-of-squares method and were then normalized with the sine value of the flip angle. The flip angle maps were obtained using the DREAM sequence. The inverse g-factor maps were evaluated with the acceleration factors R ranging from 2 to 6 in both the A-P direction and R-L directions. For temporal-SNR (tSNR) comparisons, single-shot GRE echo Planar Imaging (EPI) images were acquired with following parameters: TR/TE = 3000/26.6 ms, flip angle = 90°, FOV = 100 × 50 mm^2, matrix size = 128 × 64, resolution = 0.8 × 0.8 × 0.8 mm^3. For each voxel, the tSNR was calculated in MATLAB (MathWorks, Inc., Natick, MA, USA) as the mean value divided by the temporal standard deviation. The BOLD fMRI parameters were the same as for the tSNR scans.

To evaluate the coil capability of high-resolution imaging, a 2D GRE T2* weighted sequence was applied with the following parameters: TR/TE = 1671/34 ms, flip angle = 30°, FOV = 180 × 180 mm^2, matrix size = 896 × 896, spatial resolution = 0.2 × 0.2 × 1 mm^3, receiver bandwidth = 30 Hz/pixel, and scan time = 12 min and 49 s. The VASO sequence was based on a 2D-EPI implementation. Slice-selective slab-inversion concurrent measures of VASO and BOLD signals were acquired using a 5T scanner with the following parameter: TR_{pair}/TE = 4700/27 ms, TI-1/TI-2 = 1300/3700 ms, resolution = 0.8 × 0.8 × 1.5 mm^3, GRAPPA = 3. The imaging slice aligned to be perpendicular to the cortical layers of the hand representation in the left motor cortex. This study was approved by the Human Experiment Ethics Management Committee of Shenzhen Institute of Advanced Technology, Chinese Academy of Sciences (no. SIAT-IRB-230928-H0673). All participants provided written informed consent.

For BOLD fMRI analysis, the acquired imaging data were preprocessed and analyzed using Statistical Parametric Mapping 12 (SPM12) (Wellcome Centre for Human Neuroimaging, London, UK). Each participant's EPI images were corrected for geometric distortions caused by susceptibility-induced field inhomogeneity. All functional brain volumes were realigned to the first volume and spatially normalized to a standard stereotactic space using the template in the Montreal Neurological Institute (MNI) space. The data were high pass-filtered with a time constant of 128 s. Multiple comparisons were corrected using the false discovery rate method, resulting in a corrected voxel-level significance of $P < 0.05$.

For layer-specific analysis, concomitantly acquired time series consisting of blood-nulled and BOLD contrasts were separately corrected for motion using SPM12 (Wellcome Department of Imaging Neuroscience). Motion-corrected time series were corrected for BOLD contaminations by means of dynamically dividing blood-nulled signals with not-nulled BOLD signals using LayNii's v2.2.1 LN_BOCO[57]. In order to mitigate non-steady-state effects (transients of hemodynamic response), the division was performed on a twofold temporally upsampled time series. This form of BOLD correction in SS-SI VASO was originally developed for 7T layer fMRI and was based on the assumption that the VASO T1-contrast (in the Mz direction) is completely orthogonal to the BOLD T2* contrast (in the Mxy direction). Block design activation z-scores and beta estimates were extracted with FSL-FEAT software. Layerification and columnification were completed with the LN2_LAYERS program in LayNii software. Layer extraction was manually constrained to Brodmann area 4, which is an evolutionary older part of the primary motor cortex. In order to pinpoint this area, we followed previously described landmarks[58]. In short, we located the lateral part of the hand knob as the location on the precentral gyrus with the shortest curvature radius and selected the cortical patch medial to it.

Statistics and reproducibility

All statistical tests used, the sample sizes, the number of replicates, and how replicates were defined are described in the corresponding methods.

Reporting summary

Further information on research design is available in the Nature Portfolio Reporting Summary linked to this article.

Data availability

The datasets generated during the current study are available from the corresponding author upon reasonable request.

Code availability

All code is available in the following GitHub repository: https://github.com/Fsyuee/VASO.

Received: 18 April 2024; Accepted: 1 March 2025;
Published online: 22 March 2025

References

1. Desmurget, M., Song, Z., Mottolese, C. & Sirigu, A. Re-establishing the merits of electrical brain stimulation. *Trends Cogn. Sci.* **17**, 442–449 (2013).
2. Akselrod, M. et al. Anatomical and functional properties of the foot and leg representation in areas 3b, 1 and 2 of primary somatosensory cortex in humans: A 7T fMRI study. *Neuroimage*. **159**, 473–487(2017).
3. Ulmer, J. L. et al. Functional and dysfunctional sensorimotor anatomy and imaging. *Semin. Ultrasound* **36**, 220–233 (2015).

4. Kapoor, V., Besserve, M., Logothetis, N. K. & Panagiotaropoulos, T. I. Parallel and functionally segregated processing of task phase and conscious content in the prefrontal cortex. *Commun. Biol.* **1**, 215 (2018).
5. Jafari, M. et al. The human primary somatosensory cortex encodes imagined movement in the absence of sensory information. *Commun. Biol.* **3**, 757 (2020).
6. Penfield, W. & Boldrey, E. Somatic motor and sensory representation in the cerebral cortex of man as studied by electrical stimulation. *Brain* **60**, 389–443 (1937).
7. Rasmussen, T. & Penfield, W. Further studies of the sensory and motor cerebral cortex of man. *Fed Proc.* **6**, 452–460 (1947).
8. Penfield, W. Engrams in the human brain: mechanisms of memory. *Proc. R. Soc. Med.* **61**, 831–840 (1968).
9. Ma, S. et al. An fMRI dataset for whole-body somatotopic mapping in humans. *Sci. Data* **9**, 515 (2022).
10. Lotze, M. et al. fMRI evaluation of somatotopic representation in human primary motor cortex. *Neuroimage* **11**, 473–481 (2000).
11. Ogawa, S., Lee, T. M., Kay, A. R. & Tank, D. W. Brain magnetic resonance imaging with contrast dependent on blood oxygenation. *Proc. Natl. Acad. Sci. USA* **87**, 9868–9872 (1990).
12. Boillat, Y., Bazin, P. L. & van der Zwaag, W. Whole-body somatotopic maps in the cerebellum revealed with 7T fMRI. *Neuroimage* **211**, 116624 (2020).
13. Fried, I. et al. Functional organization of human supplementary motor cortex studied by electrical stimulation. *J. Neurosci.* **11**, 3656–3666 (1991).
14. Mottolese, C. et al. Mapping motor representations in the human cerebellum. *Brain* **136**, 330–342 (2013).
15. Kuehn, E. & Pleger, B. Encoding schemes in somatosensation: From micro- to meta-topography. *Neuroimage* **223**, 117255 (2020).
16. Lu, H., Golay, X., Pekar, J. J. & Zijl, P. C. M. V. Functional magnetic resonance imaging based on changes in vascular space occupancy. *Magn. Reson. Med.* **50**, 263 (2010).
17. Huber, L. et al. Slab-selective, BOLD-corrected VASO at 7 tesla provides measures of cerebral blood volume reactivity with high signal-to-noise ratio. *Magn. Reson. Med.* **72**, 137–148 (2014).
18. Huber, L. et al. Techniques for blood volume fMRI with VASO: From low-resolution mapping towards sub-millimeter layer-dependent applications. *Neuroimage* **164**, (2016).
19. Iamshchinina, P. et al. Perceived and mentally rotated contents are differentially represented in cortical depth of V1. *Commun. Biol.* **4**, 1069 (2021).
20. Kraff, O. & Quick, H. H. Radiofrequency coils for 7 Tesla MRI. *Top. Magn. Reson. Imaging* **28**, 145–158 (2019).
21. Williams, S. N., McElhinney, P. & Gunamony, S. Ultra-high field MRI: parallel-transmit arrays and RF pulse design. *Phys. Med. Biol.* **68**, 02TR02 (2023).
22. May, M. W. et al. A patient-friendly 16-channel transmit/64-channel receive coil array for combined head-neck MRI at 7 Tesla. *Magn. Reson. Med.* **88**, 1419–1433 (2022).
23. Feinberg, D. A. et al. Next-generation MRI scanner designed for ultra-high-resolution human brain imaging at 7 Tesla. *Nat. Methods* **20**, 2048–2057 (2023).
24. Pfaffenrot, V. et al. An 8/15-channel Tx/Rx head neck RF coil combination with region-specific B1+ shimming for whole-brain MRI focused on the cerebellum at 7T. *Magn. Reson. Med.* **80**, 1252–1265 (2018).
25. Orzada, S. et al. A 32-channel parallel transmit system add-on for 7T MRI. *PLoS ONE* **14**, e0222452 (2019).
26. Fiedler, T. M. et al. Performance and safety assessment of an integrated transmit array for body imaging at 7 T under consideration of specific absorption rate, tissue temperature, and thermal dose. *NMR Biomed.* **35**, e4656 (2022).
27. Clément, J., Gruetter, R. & Ipek, Ö. A combined 32-channel receive-loops/8-channel transmit-dipoles coil array for whole-brain MR imaging at 7T. *Magn. Reson. Med.* **82**, 1229–1241 (2019).
28. Avdievich, N. I. et al. Folded-end dipole transceiver array for human whole-brain imaging at 7T. *NMR Biomed.* **34**, e4541 (2021).
29. Avdievich, N. I., Solomakha, G., Ruhm, L., Henning, A. & Scheffler, K. Unshielded bent folded-end dipole 9.4 T human head transceiver array decoupled using modified passive dipoles. *Magn. Reson. Med.* **86**, 81–597 (2021).
30. Solomakha, G. A., Bosch, D., Glang, F., Scheffler, K. & Avdievich, N. I. Evaluation of coaxial dipole antennas as transceiver elements of human head array for ultra-high field MRI at 9.4T. *Magn. Reson. Med.* **91**, 1268–1280 (2024).
31. Woo, M. K. et al. Comparison of 16-channel asymmetric sleeve antenna and dipole antenna transceiver arrays at 10.5 Tesla MRI. *IEEE Trans. Med. Imaging* **40**, 1147–1156 (2021).
32. Avdievich, N. I. et al. A 32-element loop/dipole hybrid array for human head imaging at 7 T. *Magn. Reson. Med.* **88**, 1912–1926 (2022).
33. Woo, M. K. et al. A monopole and dipole hybrid antenna array for human brain imaging at 10.5 Tesla. *IEEE Antennas Wirel Propag. Lett.* **21**, 1857–1861 (2022).
34. Frost, R. et al. Markerless high-frequency prospective motion correction for neuroanatomical MRI. *Magn. Reson. Med.* **82**, 126–144 (2019).
35. Avdievich, N., Peshkovsky, A. & Kennan, R. Open half volume quadrature transverse electromagnetic coil for high field magnetic resonance imaging. *Magn. Reson. Med.* **53**, 937–943 (2005).
36. Avdievich, N. I., Peshkovsky, A. S., Kennan, R. P. & Hetherington, H. P. SENSE imaging with a quadrature half-volume transverse electromagnetic (TEM) coil at 4T. *J. Magn. Reson. Imaging* **24**, 934–938 (2006).
37. Shajan, G. et al. A 16-channel dual-row transmit array in combination with a 31-element receive array for human brain imaging at 9.4 T. *Magn. Reson. Med.* **71**, 870–879 (2014).
38. Sengupta, S. et al. A specialized multi-transmit head coil for high resolution fMRI of the human visual cortex at 7T. *PLoS ONE* **11**, e165418 (2016).
39. Nikulin, A. V. et al. Open birdcage coil for head imaging at 7T. *Magn. Reson. Med.* **86**, 2290–2300 (2021).
40. Wiggins, G. C. et al. 32-channel 3 Tesla receive-only phased-array head coil with soccer-ball element geometry. *Magn. Reson. Med.* **56**, 216–223 (2006).
41. Keil, B. et al. A 64-channel 3T array coil for accelerated brain MRI. *Magn. Reson. Med.* **70**, 248–258 (2013).
42. Wiggins, G. C. et al. 96-channel receive-only head coil for 3 Tesla: design optimization and evaluation. *Magn. Reson. Med.* **62**, 754–762 (2009).
43. Wei, Z. et al. 5T magnetic resonance imaging: radio frequency hardware and initial brain imaging. *Quant. Imaging Med. Surg.* **13**, 3222–3240 (2023).
44. Gruber, B. et al. A 128-channel receive array for cortical brain imaging at 7 T. *Magn Reson Med.* **90**, 2592–2607 (2023).
45. Winkler, S. A. et al. Evaluation of a flexible 12-channel screen-printed pediatric MRI coil. *Radiology* **291**, 180–185 (2019).
46. Corea, J. R. et al. Screen-printed flexible MRI receive coils. *Nat. Commun.* **7**, 10839 (2016).
47. Zhang, B., Sodickson, D. K. & Cloos, M. A. A high-impedance detector-array glove for magnetic resonance imaging of the hand. *Nat. Biomed. Eng.* **2**, 708 (2018).
48. Zhang, B. et al. Twenty-four-channel high-impedance glove array for hand and wrist MRI at 3T. *Magn. Reson. Med.* **87**, 2566–2575 (2022).
49. McGee, K. P. et al. Characterization and evaluation of a flexible MRI receive coil array for radiation therapy MR treatment planning using highly decoupled RF circuits. *Phys. Med. Biol.* **63**, 08NT02 (2018).

50. Cogswell, P. M. et al. Application of adaptive image receive coil technology for whole-brain imaging. *Am. J. Roentgenol.* **216**, 552–559 (2021).
51. Da Costa, S., Clément, J., Gruetter, R. & Ipek, Ö. Evaluation of the whole auditory pathway using high-resolution and functional MRI at 7T parallel-transmit. *PLoS ONE* **16**, e0254378 (2021).
52. Mao, T. et al. Long-range neuronal circuits underlying the interaction between sensory and motor cortex. *Neuron* **72**, 111–123 (2011).
53. Huber, L. et al. Sub-millimeter fMRI reveals multiple topographical digit representations that form action maps in human motor cortex. *Neuroimage* **208**, 116463 (2020).
54. Heeger, D. J. & David, R. What does fMRI tell us about neuronal activity? *Nat. Rev. Neurosci.* **3**, 142–151 (2002).
55. Hoult, D. I. The NMR receiver: a description and analysis of design. *Prog. Nucl. Magn. Reson. Spectrosc.* **12**, 41–77 (1978).
56. Gabriel, S., Lau, R. W. & Gabriel, C. The dielectric properties of biological tissues: III. Parametric models for the dielectric spectrum of tissues. *Phys. Med. Biol.* **41**, 2271–2293 (1996).
57. Gulban, O. F. et al. Mesoscopic in vivo human T2* dataset acquired using quantitative MRI at 7 Tesla. *Neuroimage* **264**, 119733 (2022).
58. Huber, L. et al. High-resolution CBV-fMRI allows mapping of laminar activity and connectivity of cortical input and output in human M1. *Neuron* **96**, 1253–1263 (2017).

Acknowledgements

This work was supported in part by Project on National Key Research and Development Program of China (2023YFF0714200); Strategic Priority Research Program of the Chinese Academy of Sciences (XDB0930000); Global Common Challenges of Chinese Academy of Sciences (321GJHZ2022081GC); National Natural Science Foundation of China (U22A20344, 62103404, 62271474, and 52293425); Youth Innovation Promotion Association of CAS (Y2021098); the Key Laboratory for Magnetic Resonance and Multimodality Imaging of Guangdong Province (2023B1212060052); Natural Science Foundation of Guangdong Province (2024A1515010401, 2024B1212010010); Shenzhen Overseas Innovation Team Project (KQTD20180413181834876); Shenzhen Science and Technology Program (JCYJ20210324101402008, RCYX20231211090408016, JCYJ20210324115810030, and GJHZ20210705141405016); Scientific Instrument Developing Project of the Chinese Academy of Sciences, Grant No. PTYQ2024BJ0001; the Key Laboratory of Biomedical Imaging Science and System, Chinese Academy of Sciences; State Key Laboratory of Biomedical Imaging Science and System.

Author contributions

Ye Li and JingLong Wu conceived the project and supervised the project. Zidong Wei modeled the head coil, tested and compared the image quality of the coil, and wrote the first draft of the paper. Zhilin Zhang designed the methodology and experiment to validate the coil. Qiaoyan Chen analyzed the SNR of the image. Cuiting Wang debugs the MRI sequence and helps with data acquisition. Shuyue Fu collected the coil data and analyzed the data. Xiaoliang Zhang and Haifeng Wang advised on fMRI data analysis. Xin Liu and Hairong Zheng provided suggestions and assistance for the coil design.

Competing interests

The authors declare no competing interests.

Additional information

Supplementary information The online version contains supplementary material available at https://doi.org/10.1038/s42003-025-07866-7.

Correspondence and requests for materials should be addressed to Jinglong Wu or Ye Li.

Peer review information *Communications Biology* thanks Akbar Alipour, Alexander Beckett, and the other, anonymous, reviewer(s) for their contribution to the peer review of this work. Primary Handling Editors: Dr Sahar Ahmad and Dr Ophelia Bu. A peer review file is available.